






Differential phosphorylation of Clr4^{SUV39H} by Cdk1 accompanies a histone H3 methylation switch that is essential for gametogenesis

Tahsin Kuzdere^{1,2} , Valentin Flury^{1,2} , Thomas Schalch³ , Vytautas Iesmantavicius¹, Daniel Hess¹  & Marc Bühler^{1,2,*} 

Abstract

Methylation of histone H3 at lysine 9 (H3K9) is a hallmark of heterochromatin that plays crucial roles in gene silencing, genome stability, and chromosome segregation. In *Schizosaccharomyces pombe*, Clr4 mediates both di- and tri-methylation of H3K9. Although H3K9 methylation has been intensely studied in mitotic cells, its role during sexual differentiation remains unclear. Here, we map H3K9 methylation genome-wide during meiosis and show that constitutive heterochromatin temporarily loses H3K9me2 and becomes H3K9me3 when cells commit to meiosis. Cells lacking the ability to tri-methylate H3K9 exhibit meiotic chromosome segregation defects. Finally, the H3K9 methylation switch is accompanied by differential phosphorylation of Clr4 by the cyclin-dependent kinase Cdk1. Our results suggest that a conserved master regulator of the cell cycle controls the specificity of an H3K9 methyltransferase to prevent ectopic H3K9 methylation and to ensure faithful gametogenesis.

Keywords chromosome segregation; fission yeast; histone methylation; meiosis; phosphorylation

Subject Categories Cell Cycle; Post-translational Modifications & Proteolysis

DOI 10.15252/embr.202255928 | Received 8 August 2022 | Revised 18 October 2022 | Accepted 27 October 2022 | Published online 21 November 2022

EMBO Reports (2023) 24: e55928

Introduction

H3K9 methylation is a hallmark of heterochromatin that functions in chromatin-dependent gene silencing and maintenance of genome stability by repressing repetitive DNA elements and recruiting downstream factors essential for faithful chromosome segregation (Lachner & Jenuwein, 2002; Martin & Zhang, 2005; Bloom, 2014). Fundamental principles of these processes have been elucidated in the fission yeast *Schizosaccharomyces pombe*, in which Clr4, the homolog of mammalian SUV39H, is the sole

known H3K9 methyltransferase. Whereas H3K9 methylation has been intensely studied in mitotic cells (Grewal & Jia, 2007; Allshire & Ekwall, 2015), its role during sexual differentiation is less well understood.

Schizosaccharomyces pombe grows and divides mitotically in nutrient-rich conditions. Upon nitrogen starvation and availability of a mating partner, meiosis is initiated where a premeiotic S-phase is followed by the first and second meiotic division, producing four haploid gametes (Yamashita *et al.*, 2017). It is well established that the heterochromatic state of centromeres and telomeres is important during meiosis (Chikashige *et al.*, 1994; Watanabe & Nurse, 1999; Hall *et al.*, 2003; Ellermeier *et al.*, 2010). In particular, the fission yeast heterochromatin protein 1 (HP1) homolog Swi6, which specifically binds H3K9 methylated nucleosomes through its chromodomain (CD) (Ekwall *et al.*, 1995; Bannister *et al.*, 2001), exhibits important roles during gametogenesis. During meiotic progression, Swi6 does not only physically bridge between pericentromeric H3K9 methylation and the meiosis-specific cohesin complex but also promotes kinetochore assembly and correct temporal attachment of sister chromatids during the meiotic divisions (Bernard *et al.*, 2001; Nonaka *et al.*, 2002; Kitajima *et al.*, 2003; Yamagishi *et al.*, 2008). Consequently, *clr4^Δ* cells, which are devoid of heterochromatin, exhibit lagging chromosomes and defective microtubule attachment to kinetochores during meiotic divisions (Kitajima *et al.*, 2003; Klutstein *et al.*, 2015).

It has recently become clear that di- and tri-methylation of H3K9 (H3K9me2 and H3K9me3, respectively) can define functionally distinct chromatin states. H3K9me3 domains are associated with high levels of HP1 proteins and are poorly transcribed, whereas H3K9me2 marked heterochromatin is transcriptionally permissive (Jih *et al.*, 2017). Whereas H3K9me2 and H3K9me3 co-exist in mitotically growing wild-type cells, mutant cells expressing a hyperactive form of Clr4 were shown to have higher H3K9me3 levels and to form illegitimate, ectopic heterochromatin (Iglesias *et al.*, 2018). Whether such a shift towards one of the two H3K9 methylation states could occur in wild-type cells, under physiological conditions, remains unknown.

1 Friedrich Miescher Institute for Biomedical Research, Basel, Switzerland

2 University of Basel, Basel, Switzerland

3 Department of Molecular and Cell Biology, Leicester Institute of Structural and Chemical Biology, University of Leicester, Leicester, UK

*Corresponding author. Tel: +41 616976651; E-mail: marc.buehler@fmi.ch

Similarly, the spatial and temporal distribution of the H3K9me2 and H3K9me3 marks in meiotic cells, and their functional relevance have not been elucidated. Here, we map H3K9 methylation genome-wide during meiosis and show that constitutive heterochromatin temporarily loses H3K9me2 and becomes H3K9me3 when cells commit to meiosis. Cells lacking the ability to tri-methylate H3K9 exhibit meiotic chromosome segregation defects, which does not occur in mitotic cells. This results in the production of less viable spores. Artificially increasing the affinity of Swi6 towards H3K9me2 rescues spore viability and chromosome segregation in the absence of H3K9me3. Finally, we show that the H3K9 methylation switch is accompanied by differential phosphorylation of Ctr4, mediated by the cyclin-dependent kinase (CDK) Cdk1. This suggests that Cdk1 could regulate the specificity of Ctr4, thereby controlling the ratio of H3K9me2 to H3K9me3 to prevent ectopic H3K9 methylation and to ensure faithful meiotic chromosome segregation.

Results

H3K9me2 switches to H3K9me3 at the onset of gametogenesis

To profile the heterochromatic landscape during meiosis we performed chromatin immunoprecipitation followed by high throughput sequencing (ChIP-seq) at hourly intervals in diploid *S. pombe* cells undergoing synchronous meiosis (Cipak *et al*, 2014; Figs 1A and EV1A and B). When comparing the genome-wide distribution of H3K9me2 and H3K9me3 marks between mitotic and early meiotic *ctr4⁺/ctr4⁺* cells, we did not observe any facultative heterochromatin sites (Figs 1B and EV2A). However, we noticed a loss of H3K9me2 at the centromeres, telomeres, and subtelomeres at 1 h into meiosis. The decrease of H3K9me2 was accompanied by an increased H3K9me3 signal at these sites (Fig 1B). This anticorrelation was also observed after normalization to mouse embryonic stem cell

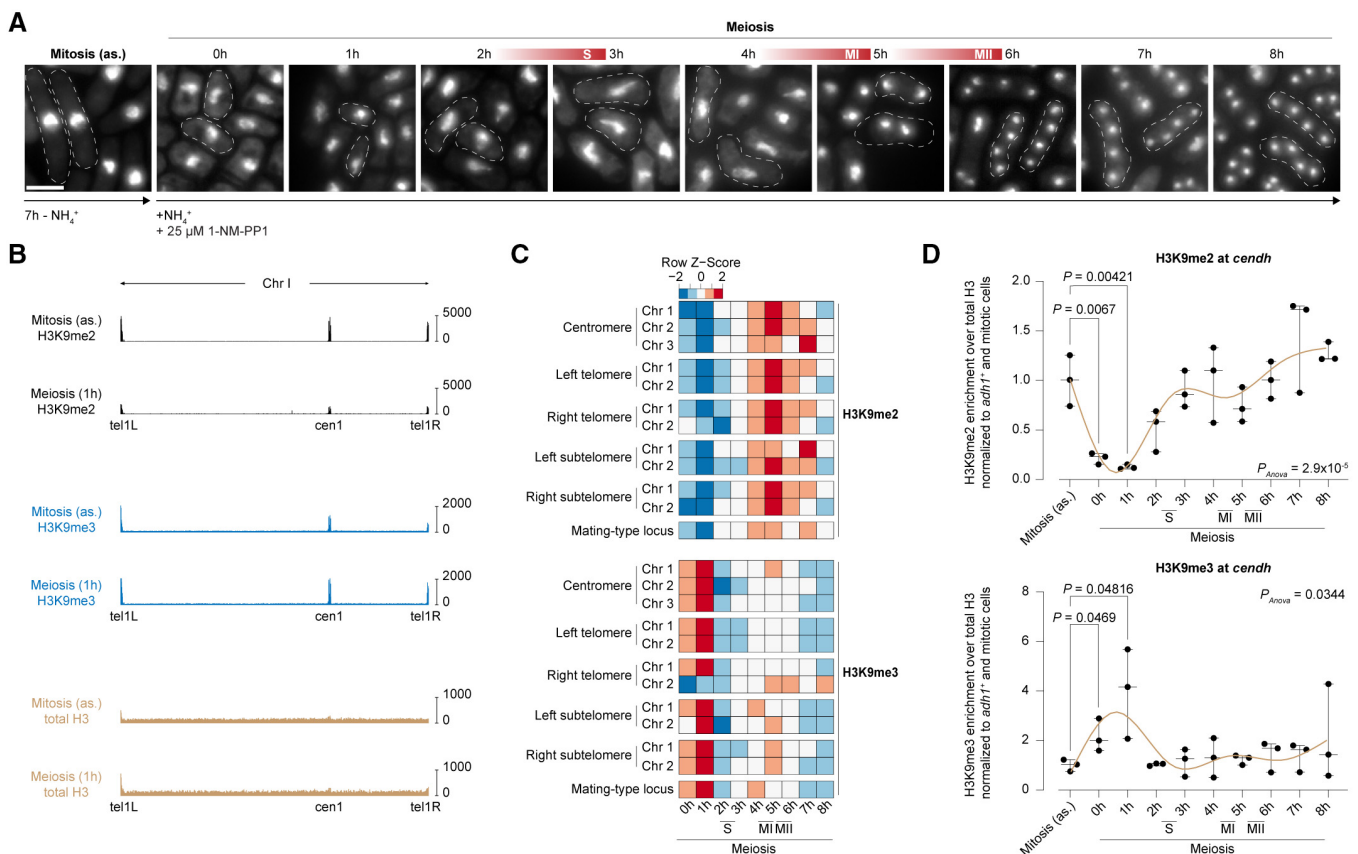


Figure 1. H3K9me2 transitions to H3K9me3 at the onset of meiosis.

A Exemplary images of ethanol-fixed and DAPI-stained *pat1-as2/pat1-as2 mat-Pc* cells synchronized for meiotic progression. 0 h corresponds to cells after 7 h of premeiotic nitrogen starvation and marks the start of nitrogen and 1-NM-PP1 addition. The timing of premeiotic S-phase (S), meiosis I (MI), and meiosis II (MII) are indicated above the images; Scale bar = 5 μ m.

B Genome browser snapshot of H3K9me2 (black), H3K9me3 (blue), and total H3 (brown) ChIP-seq reads in asynchronous mitotic and early meiotic (1 h) cells mapped to chromosome I. Reads were normalized to library size and are shown as reads per million; cen1, centromere 1; tel1L, left telomere 1; tel1R, right telomere 1.

C H3K9me2 (top) and H3K9me3 (bottom) ChIP-seq enrichments (scaled) at constitutive heterochromatin regions during meiotic progression. Multi-mapping reads were normalized to library size and total H3 ChIP-seq enrichments. Two independent biological replicates were sequenced and the average enrichment is displayed.

D ChIP-qPCR experiments to assess H3K9me2 (top) and H3K9me3 (bottom). Levels at pericentromeric repeats (*centh*) during mitosis and meiosis. ChIP enrichments were normalized to total H3 levels and *adh1⁺* and are shown relative to mitotic cells; error bars, s.d.; $n = 3$ independent biological replicates; P values between two time points were calculated using a two-tailed student's t -test, P_{ANOVA} was calculated using ANOVA.

chromatin, which we used as an exogenous spike-in control (Fig EV2B). We observed elevated H3K9me3 levels at all constitutive heterochromatin regions during early meiosis (0–1 h), which started to decrease after 2 h, as H3K9me3 was replaced by H3K9me2 (Figs 1C and EV2C). Intrigued by the anticorrelation of H3K9me2 and H3K9me3 marks at the onset of meiosis, we performed ChIP–qPCR experiments to validate H3K9me2 to H3K9me3 ratios at centromeres. Following the entry into meiosis (1 h), H3K9me2 levels declined and H3K9me3 levels rose at the pericentromeric repeats. As meiosis progressed, the H3K9me2 signal was restored gradually reaching mitotic enrichment levels after 6–8 h, which was mirrored by a decline in H3K9me3 (Fig 1D). In conclusion, though we found no evidence for *de novo* formation of facultative heterochromatin during meiosis, we discovered an unanticipated H3K9 methylation switch that occurs at the onset of gametogenesis.

H3K9me3 is required for meiotic chromosome segregation

To gain insights into the physiological relevance of the observed H3K9 methylation switch, we created diploid cells carrying a homozygous active-site mutation in Clr4 (Clr4^{F449Y}), which allows the generation of H3K9me2 but blocks its conversion to H3K9me3 (Jih et al, 2017). Consistent with a failure to convert H3K9me2 to H3K9me3, diploid *clr4^{F449Y}/clr4^{F449Y}* cells displayed strongly elevated H3K9me2 levels when in mitosis, while H3K9me3 was absent (Figs 2A and EV3A). In contrast to wild-type cells, H3K9me2 levels remained high and were unaffected in *clr4^{F449Y}/clr4^{F449Y}* cells when entering meiosis (Fig 2B and C). This experiment confirms that the waning of H3K9me2 during early meiosis is not an artifact caused by the synchronization protocol. It also supports a model in which H3K9me2 is effectively converted to H3K9me3 at the onset of meiosis in wild-type cells, rather than being removed by an H3K9me2-specific demethylase. That some residual, nonconverted H3K9me2 vanishes through active removal or nucleosome loss remains a possibility though.

Chromosomes do not segregate properly in both mitotic and meiotic *clr4^Δ* cells, which are devoid of pericentromeric heterochromatin (Ekwall et al, 1996; Yamagishi et al, 2008; Klutstein

et al, 2015). When monitoring mitotically growing *clr4^{F449Y}* cells, we observed no reduction in the growth rate and there was no increased sensitivity to the microtubule-destabilizing drug thiabendazole (TBZ) (Fig EV3B and C). We also did not observe any obvious lagging DNA patterns, which are hallmarks of impaired chromosome segregation (Pidoux et al, 2000; Fig 3A). Thus, H3K9me3 at the pericentromeric repeats is dispensable for segregating chromosomes during mitosis. To investigate whether the aforementioned H3K9 methylation switch could be important for the proper execution of the meiotic program, we monitored chromosome segregation patterns after mating homothallic *clr4^{F449Y}* cells by light microscopy. *clr4^{F449Y}/clr4^{F449Y}* cells displayed lagging DNA during the first meiotic division in more than 20% of cells monitored, which we also observed in *clr4^Δ/clr4^Δ* cells but much less frequently in wild-type cells (Fig 3B). To assess whether this potential abnormality leads to defects in chromosome segregation during meiosis, we examined the segregation of GFP-tagged centromeres (CenI-GFP) (Nabeshima et al, 1998) during meiosis I (MI) and meiosis II (MII) in dyads and tetrads from diploid cells that were heterozygous for the *cenI-GFP* marker (Fig 3C and D). Indeed, the distribution of the GFP dots revealed aberrant segregation of sister chromatids in MI of *clr4^{F449Y}/clr4^{F449Y}* cells, with a high frequency of equational segregation that normally occurs during MII (Fig 3D). This is different from *clr4^Δ/clr4^Δ* cells, in which sister chromatids were reported to co-segregate normally (reductional segregation) during the first but not the second meiotic division (equational segregation) in cells lacking Clr4 (Kitajima et al, 2003). We observed GFP dot distributions that are indicative of defective MI segregation also in Clr4-deficient tetrads, but this was not significantly different from wild-type cells (Fig 3E, yellow fraction). Consistent with earlier findings, we frequently observed spores with two GFP dots in a single nucleus of a tetrad derived from *clr4^Δ/clr4^Δ* cells (Fig 3E, green fraction). Such a pattern (i.e., normal segregation during MI but not MII) occurred in < 1% of *clr4^{F449Y}/clr4^{F449Y}* cells that we have analyzed (Fig 3E). Thus, cells that cannot fully transition to H3K9me3 at the onset of meiosis show a unique MI-specific mutant phenotype that is different from cells lacking H3K9 methylation completely.

Finally, we assessed spore viability in cells lacking H3K9me3 by tetrad microdissection. As anticipated when chromosome

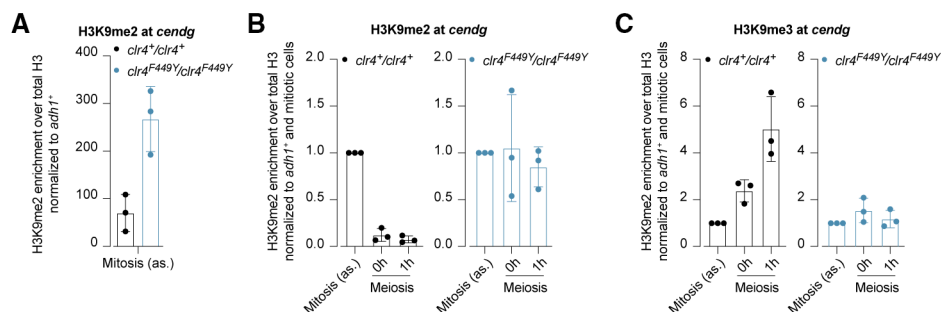


Figure 2. *clr4^{F449Y}/clr4^{F449Y}* cells fail to convert H3K9me2 to H3K9me3 at the onset of meiosis.

- A ChIP–qPCR experiments to assess mitotic H3K9me2 levels at pericentromeric repeats (*cendg*) in *clr4⁺/clr4⁺* (black) and *clr4^{F449Y}/clr4^{F449Y}* (blue) cells. ChIP enrichments were normalized to total H3 levels and *adh1⁺*; error bars, s.d.; $n = 3$ independent biological replicates.
- B, C ChIP–qPCR experiments to assess H3K9me2 (B) and H3K9me3 (C) levels at pericentromeric repeats (*cendg*) in *clr4⁺/clr4⁺* (black) and *clr4^{F449Y}/clr4^{F449Y}* (blue) cells during mitosis and early meiosis. ChIP enrichments were normalized to total H3 levels and *adh1⁺* and are shown relative to mitotic cells; error bars, s.d.; $n = 3$ independent biological replicates.

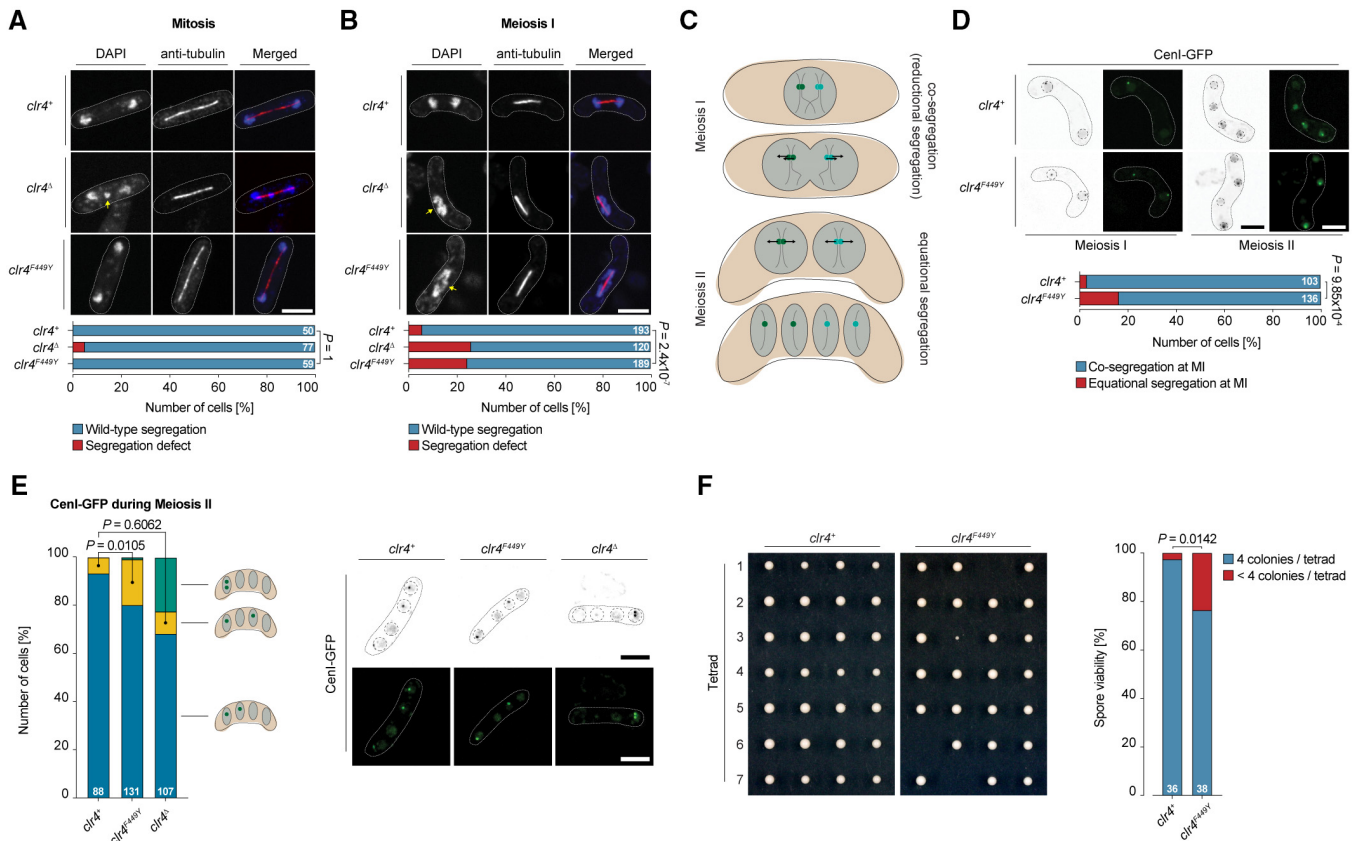


Figure 3. H3K9me3 is dispensable for proper mitotic but not meiotic chromosome segregation.

A, B Comparison of requirement for H3K9 methylation for mitotic (A) and meiotic (B) chromosome segregation. Exemplary IF microscopy images of the indicated fission yeast strains are shown. Homothallic strains were grown either in rich medium (A) or incubated on SPAS plates (B). DNA and tubulin were stained with DAPI and anti-TAT-1, respectively. Lagging DNA is indicated with a yellow arrow; Scale bar = 5 μ m. Quantification of chromosome segregation phenotypes is shown below the microscopy images. P values were calculated using Fisher's exact test. Number of total cells counted is indicated in each bar.

C Schematic illustration showing the distribution of sister chromatids (green and turquoise dots, respectively) during meiotic divisions. In wild-type cells, sister chromatids first co-segregate (reductional segregation) during MI and then undergo equational segregation during MII. Therefore, sister chromatids end up in adjacent ascospores after the second meiotic division.

D Comparison of requirement for H3K9me3 for co-segregation of centromere I (CenI) during MI. Exemplary live cell microscopy images of the indicated fission yeast strains during MI and MII are shown. Heterothallic strains were crossed and dyads, as well as tetrads were subjected to the analysis. Heterozygous CenI-GFP was used to determine the segregation pattern during meiosis. The GFP signal is additionally displayed in greyscale for better visibility; Scale bar = 5 μ m. Quantifications of CenI-GFP segregation are shown below the microscopy images. P values were calculated using Fisher's exact test. Number of total cells counted is indicated in each bar.

E Comparison of requirement for H3K9 methylation for CenI distribution after MII. Quantification of CenI distribution (left) and exemplary images (right) of the indicated fission yeast strains are shown. Heterothallic strains were crossed and resulting tetrads were analyzed. Heterozygous CenI-GFP was used to classify the distribution of CenI after MII. The GFP signal is additionally displayed in greyscale for better visibility; Scale bar = 5 μ m. P values were calculated using Fisher's exact test. Number of total cells counted is indicated in each bar.

F Tetrad dissection to assess spore viability in *clr4+* and *clr4^{F449Y}* cells. Meiosis was induced in homothallic cells and the resulting spores were dissected. Exemplary images (left) and quantifications of spore viability (right) are shown. P values were calculated using Fisher's exact test. Number of dissected tetrads is indicated in each bar.

segregation is disturbed during meiosis, spores from homozygous *clr4^{F449Y}* tetrads recurrently failed to form colonies (Fig 3F). Thus, we conclude that the H3K9 methylation switch occurring at the onset of fission yeast meiosis is essential for gametogenesis.

Meiotic phenotypes caused by a lack of H3K9me3 are rescued by increased Swi6 affinity towards H3K9me2

Methylated H3K9 serves as a binding site for proteins with a CD, whose binding affinity is positively correlated with the methylation

state of the histone tail (me1 < me2 < me3) (Eissenberg, 2012). Swi6 is such a protein and is known to regulate chromosome segregation by recruiting cohesin, promoting kinetochore assembly, and preventing inaccurate microtubule attachment (Bernard *et al*, 2001; Yamagishi *et al*, 2008). To assess Swi6 binding to centromeres in wild-type and *clr4* mutant cells during MI, we performed live cell fluorescence microscopy with cells expressing Swi6-yeGFP and a centromere marker, Mis6-mCherry. Consistent with earlier studies, the majority of Swi6 colocalized with centromeres during MI in *clr4+/clr4+* cells. Furthermore, DNA was pulled to the opposite poles

of the cell with a subset of telomere-bound Swi6 foci trailing behind (Klutstein *et al*, 2015). In *clr4^Δ/clr4^Δ* cells, no distinct Swi6-yeGFP localization, but a rather diffuse nuclear staining was observed. Similarly, the majority of Swi6-yeGFP signal was evenly distributed in the nucleus of H3K9me3-deficient *clr4^{F449Y}/clr4^{F449Y}* cells, with only a small fraction colocalizing with centromeres (Fig 4A). This observation indicates that highest binding affinity of Swi6 towards H3 is necessary for proper subnuclear localization in meocytes, for which H3K9 needs to be tri-methylated.

Previous studies have shown that binding of Swi6 to dimethylated histone H3-tail peptides is roughly threefold lower compared with tri-methylated peptides (10.28 and 3.34 μ M, respectively; Schalch *et al*, 2009). This raises the possibility that the H3K9

methylation switch at the onset of meiosis could function to increase the affinity of Swi6 for pericentromeric nucleosomes. To test whether increased affinity of Swi6 towards H3K9me2 would rescue the meiotic segregation defects of a *clr4^{F449Y}* strain, we mutated key residues in the CD of Swi6 (E80V, V82E, S116E, D120N, S122F), making it more similar to the high-affinity CD of the fission yeast telomere-binding protein 1 (Chp1; 0.55 μ M for H3K9me2; Schalch *et al*, 2009). Substituting Swi6 with Swi6^{Chp1-like-CD} in the *clr4^{F449Y}/clr4^{F449Y}* background restored Swi6 binding and enrichments at the pericentromeric repeats (Fig 4A and B). Furthermore, fewer *clr4^{F449Y}/clr4^{F449Y}* cells displayed lagging DNA upon expression of Swi6^{Chp1-like-CD} (Fig 4C and D). Also, co-segregation of sister chromatids in MI was significantly improved when Swi6^{Chp1-like-CD} was

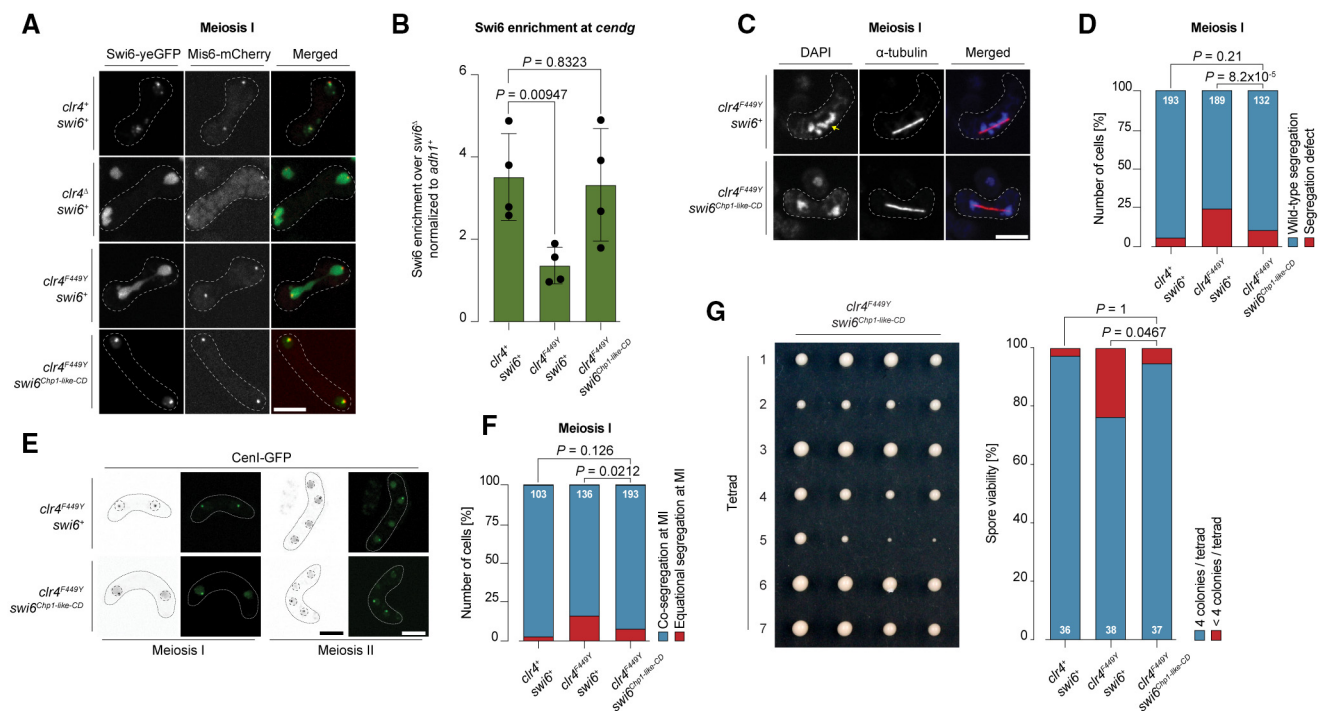


Figure 4. Restoration of Swi6 binding to pericentromeric repeats rescues the meiotic chromosome segregation phenotype in H3K9me3-depleted cells.

- A Comparison of Swi6 localization depending on H3K9 methylation during MI. Exemplary live cell microscopy images of the indicated fission yeast strains are shown. Homothallic strains were spotted on SPAS plates before being mounted on microscopy slides. Swi6, Swi6^{Chp1-like-CD}, and the centromere marker Mis6 were visualized by tagging with yeGFP and mCherry, respectively; Scale bar = 5 μ m.
- B ChIP-qPCR experiment to assess Swi6 levels at the pericentromeric repeats (*cendg*) in the indicated fission yeast strains during mitosis. ChIP enrichments were normalized to *adh1⁺* and are shown relative to *swi6^Δ* cells; error bars, s.d.; $n = 4$ independent biological replicates. P values were calculated using a two-tailed student's t -test.
- C Comparison of meiotic chromosome segregation in cells lacking H3K9me3 depending on Swi6's affinity towards H3K9me2. Exemplary IF microscopy images of the indicated fission yeast strains are shown. Homothallic strains were incubated on SPAS plates. DNA and tubulin were stained with DAPI and anti-TAT-1, respectively. Missegregating chromosome is indicated with a yellow arrow; Scale bar = 5 μ m.
- D Quantification of meiotic chromosome segregation phenotypes. The data for *clr4^Δ* and *clr4^{F449Y}* is the same as shown in Fig 3B. P values were calculated using Fisher's exact test. Number of total cells counted is indicated in each bar.
- E Comparison of co-segregation of centromere I (CenI) during MI and II in cells lacking H3K9me3 depending on Swi6's affinity towards H3K9me2. Exemplary live cell microscopy images of the indicated fission yeast strains during MI and MII are shown. Heterothallic strains were crossed and dyads, as well as tetrads were subjected to the analysis. Heterozygous CenI-GFP was used to follow the segregation pattern during meiosis. The GFP signal is additionally displayed in greyscale for better visibility; Scale bar = 5 μ m.
- F Quantification of CenI-GFP segregation during meiosis. The data for *clr4^Δ* and *clr4^{F449Y}* is the same as shown in Fig 3D. P values were calculated using Fisher's exact test. Number of total cells counted is indicated in each bar.
- G Tetrad dissection to assess spore viability in *clr4^{F449Y} swi6^{Chp1-like-CD}* cells. Exemplary image (left) and quantification of the spore viability (right) are shown. Meiosis was induced in homothallic cells and the resulting spores were dissected. The data for *clr4^Δ* and *clr4^{F449Y}* is the same as shown in Fig 3F. P values were calculated using Fisher's exact test. Number of dissected tetrads is indicated in each bar.

expressed in *clr4^{F449Y}/clr4^{F449Y}* cells (Fig 4E and F), and spores formed colonies again (Fig 4G).

These results suggest that the *in vivo* affinity of Swi6 towards H3K9me2 is not strong enough to fulfill its roles during early meiosis. This is peculiar because chromosomes are generally assumed to segregate normally during MI, and randomly during MII, in cells lacking Clr4 (Kitajima *et al*, 2003). This highlights that the exact roles of heterochromatin during meiotic chromosome segregation are not fully understood. We therefore advocate for revisiting mechanistic studies on the role of heterochromatin during meiosis, with a particular focus on reductional chromosome segregation during MI, for which the *clr4^{F449Y}* allele (Jih *et al*, 2017) will be very powerful.

Excessive H3K9 methyl binding affinity of Swi6 causes formation of ectopic H3K9me2 islands

The results described above pose the question why Swi6 did not simply evolve to have a higher affinity towards H3K9me2 rather than requiring a change from H3K9me2 to H3K9me3 in early meiosis. Therefore, we investigated what consequences a higher binding affinity of Swi6 would have in mitotically growing cells by performing ChIP-seq experiments in various Swi6 and Clr4 mutant backgrounds. Consistent with the live cell imaging results, little Swi6 was bound at the centromeric repeats in *clr4^{F449Y}* cells (Fig 5A). Because telomeric H3K9me2 cannot be stably maintained by Clr4^{F449Y}, Swi6 was no longer enriched at telomeres (Fig EV4A; Jih *et al*, 2017). However, centromeric Swi6^{Chp1-like-CD} binding was restored (Fig 5A). In *clr4⁺* cells, Swi6^{Chp1-like-CD} was strongly enriched at the pericentromeric repeats but completely lost in cells lacking H3K9 methylation (Fig EV4B and C). Moreover, Swi6^{Chp1-like-CD} was ectopically binding at many sites distributed over the genome in *clr4⁺* cells, which was accompanied by the formation of the H3K9me2 islands at those sites (Fig 5A and B).

These results show that increasing Swi6's affinity towards methylated H3K9 beyond physiological levels can lead to ectopic H3K9 methylation in mitotic cells. Therefore, it is desirable to have a low-affinity Swi6 protein, as this would firstly prevent unwanted H3K9 methylation in regions with potential nucleation sites, and secondly provide the organism a means to recruit effector proteins conditionally through modulation of the H3K9 methylation state in a fast and reversible manner. Notably, neither did we observe H3K9me3 at the ectopic, Swi6^{Chp1-like-CD} bound H3K9me2 islands (Fig 5A and B), nor was gene expression different at these sites in *swi6⁺* and *swi6^{Chp1-like-CD}* cells (Fig 5C). This corroborates earlier findings that H3K9 methylation is not repressive *per se* (Duempelmann *et al*, 2019), and suggests that additional mechanisms must be activated to silence facultative H3K9me2 islands in *S. pombe*.

Clr4 is differentially phosphorylated during meiosis

Clr4 histone methyltransferase activity is intrinsically inhibited in mitotic cells by an autoregulatory loop (ARL) that connects the SET and post-SET domains (Iglesias *et al*, 2018). Our results imply that such inhibition is reversed at the onset of meiosis, likely via deposition or removal of a post-translational modification (PTM), which is well-known to regulate protein activities in a fast and reversible manner (Olsen *et al*, 2006). Phosphoproteomic screens in *S. pombe* revealed multiple phosphorylation sites on Clr4. Yet, biological

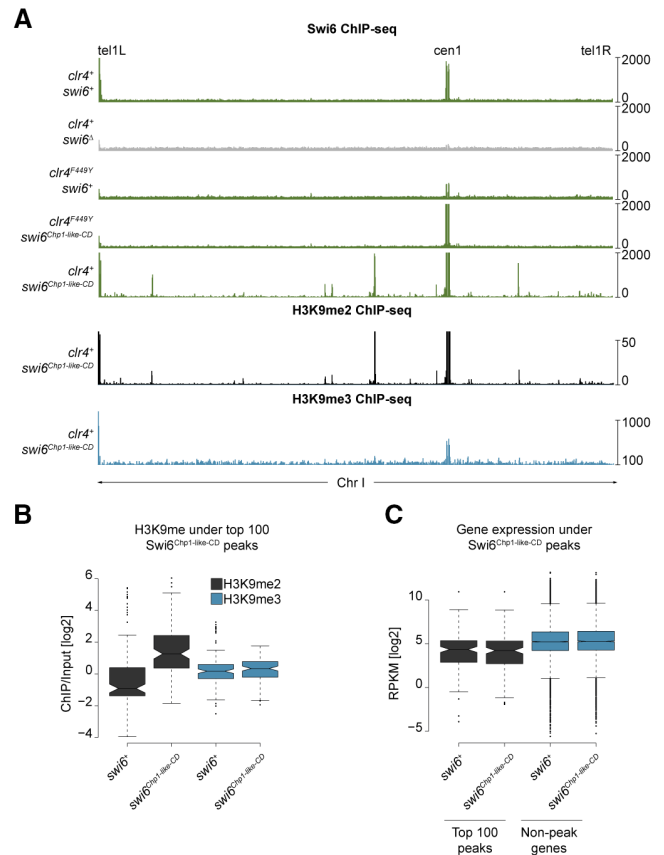


Figure 5. Increasing Swi6 binding affinity towards H3K9 methylation causes ectopic H3K9me2 formation.

- A** Genome browser snapshot of Swi6, H3K9me2, and H3K9me3 ChIP-seq reads in the indicated strains mapped to chromosome I. Reads were normalized to library size and are shown as reads per million; cen1, centromere 1; tel1L, left telomere 1; tel1R, right telomere 1.
- B** Quantification of H3K9me2 (black) and H3K9me3 (blue) enrichments at the top 100 ectopic Swi6^{Chp1-like-CD} peaks in *swi6⁺* and *swi6^{Chp1-like-CD}* cells. Input normalized ChIP enrichments are shown in log₂ scale; center line, median; boxes, first and third quartile; whiskers, maximum and minimum values of distribution; points, outliers; *n* = 2 independent biological replicates.
- C** Quantification of gene expression levels in *swi6⁺* and *swi6^{Chp1-like-CD}* cells at either the top 100 ectopic Swi6^{Chp1-like-CD} peaks (black) or random nonpeak genes (blue). Reads were normalized to gene length and to million mapped reads (RPKM) and are shown in log₂ scale; center line, median; boxes, first and third quartile; whiskers, maximum and minimum values of distribution; points, outliers; *n* = 3 independent biological replicates.

relevance has remained enigmatic (Cary *et al*, 2014; Kettenbach *et al*, 2015; Swaffer *et al*, 2018). To examine whether the phosphorylation state of Clr4 changes when cells enter meiosis, we analyzed the migration of 3xFLAG-tagged Clr4 (3xFLAG-Clr4) protein extracted from mitotic and meiotic cells on PhosTag gels. This revealed that Clr4 was dephosphorylated during early meiosis (0–1 h), and became gradually phosphorylated after 2 h into the meiotic program (Figs 6A and EV5A), correlating well with the timing of the H3K9 methylation switch (Fig 1D). To determine the differentially phosphorylated Clr4 residues, we subjected mitotic and meiotic 3xFLAG-Clr4 protein to mass spectrometry. Intriguingly,

this revealed two differentially phosphorylated serine residues, S458 and S462, which are located in the ARL of Clr4 (Fig 6B). Substituting the first serine of the ARL with a nonphosphorylatable alanine residue (Clr4^{S458A}) was sufficient to abrogate slow migration of mitotic Clr4 on PhosTag gels, mimicking migration of meiotic Clr4. Mutating S462 in addition to S458 had no noticeable additive effect (Fig 6C). Thus, S458 is a key residue of Clr4 that is differentially phosphorylated during meiosis

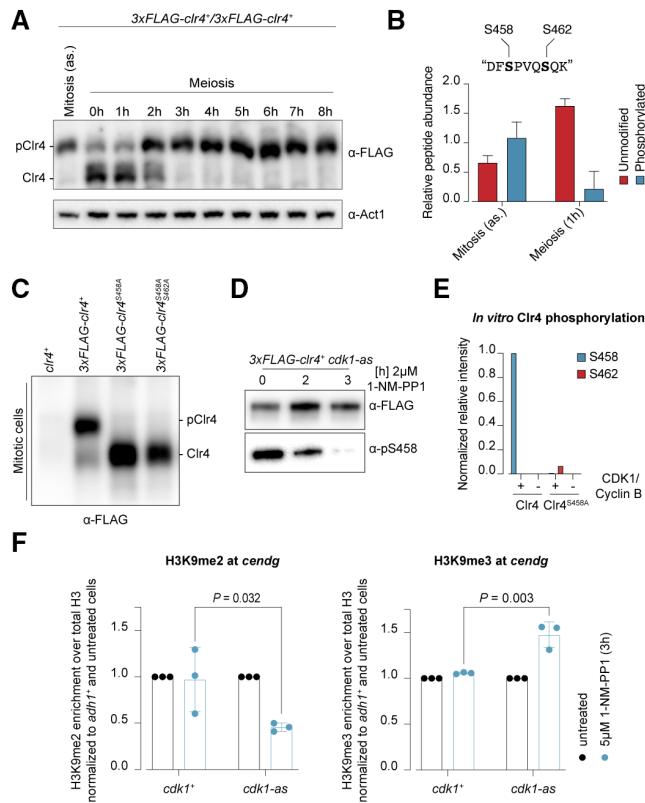


Figure 6. Clr4^{S458} is differentially phosphorylated in a Cdk1-dependent manner in mitosis versus early meiosis.

- A Western blot of whole-cell lysates (WCL) using a PhosTag gel for anti-FLAG (top) and a Bis-Tris gel for anti-Act1 detection (bottom), respectively. WCL were prepared from mitotic and meiotic *3xFLAG-clr4*⁺/*3xFLAG-clr4*⁺ cultures at the indicated time points.
- B Comparing the relative abundance of the differentially phosphorylated Clr4 peptide (DFSVPVQSQK) in mitosis and early meiosis by IP-MS; error bars, s.d.; *n* = 3 independent biological replicates.
- C Western blot of FLAG IPs using a PhosTag gel to assess phosphorylation levels of Clr4 in the indicated homoallelic strains.
- D Western blot of FLAG IPs in *3xFLAG-clr4*⁺ *cdc2-as* cells, treated with 2 μM 1-NM-PP1 for the indicated amount of time. The blot was first probed with the phospho-specific anti-pS458 antibody, stripped, and re-probed with an anti-FLAG antibody.
- E *In vitro* kinase assay of recombinant Clr4 and Clr4^{S458A} in the presence and absence of human CDK1/Cyclin B. Phosphorylation events were analyzed by mass spectrometry.
- F ChIP-qPCR experiments to assess H3K9me2 (left) and H3K9me3 (right) levels at pericentromeric repeats (*centdg*) in *cdk1*⁺ and *cdk1-as* cells treated with and without 5 μM 1-NM-PP1. ChIP enrichments were normalized to total H3 levels and *adh1*⁺ and are shown relative to untreated cells; error bars, s.d.; *n* = 3 independent biological replicates; *P* values were calculated using a two-tailed student's *t*-test.

Inhibition of Cdk1 triggers the conversion of H3K9me2 to H3K9me3

The above results support a model in which constitutive phosphorylation of Clr4 dampens H3K9me3 activity during mitosis. At the onset of meiosis, Clr4 phosphorylation at S458 ceases, enabling the full transition from H3K9me2 to H3K9me3. To identify the kinase responsible for Clr4^{S458} phosphorylation, we performed a candidate screen making use of a phospho-specific antibody that we raised against Clr4^{S458} (α-pS458) (Fig EV5B). We selected candidate kinases based on meiotic phenotypes, minimal consensus sequence preference (S/T-P), and mitotic versus meiotic expression or activity. Of those candidates who were nonessential and could be knocked out, none was accountable for Clr4 phosphorylation (Fig EV5C). One candidate that we could not delete is the cyclin-dependent kinase Cdk1 (also known as Cdc2). Instead, we used an ATP analog-sensitive *cdk1* allele (*cdk1-as*) that allows conditional inhibition of Cdk1 activity (Dischinger *et al*, 2008). Upon inhibition of Cdk1 activity, Clr4^{S458} phosphorylation rapidly decreased and was undetectable 3 h postinhibition, whereas Clr4 phosphorylation levels remained unaffected in *cdk1*⁺ cells (Figs 6D and EV5D). Thus, phosphorylation of Clr4 at S458 critically depends on Cdk1. To test whether Clr4 could be a direct target of Cdk1, we performed *in vitro* kinase assays with recombinant Clr4 and commercially available human CDK1/Cyclin B. Indeed, CDK1/Cyclin B phosphorylated recombinant Clr4 specifically at S458 (Fig 6E). To ultimately test if Cdk1 inhibition would trigger the conversion of H3K9me2 to H3K9me3, we performed ChIP experiments in mitotically growing *cdk1*⁺ and *cdk1-as* cells in the absence or presence of the ATP analog 1-NM-PP1. This revealed reduced H3K9me2, but increased H3K9me3 levels upon 1-NM-PP1 addition in *cdk1-as* cells specifically (Fig 6F), mimicking the H3K9 methylation switch naturally occurring at the onset of gametogenesis.

Discussion

Methylation of H3K9, the hallmark of heterochromatin, has been intensely studied in mitotic cells, in particular in *S. pombe*, where many fundamental principles of heterochromatin biology have been discovered and mechanistically dissected. Whereas there is a wealth of information about *S. pombe* heterochromatin in mitotic cells, startlingly little is known about it during meiosis. Also, although known for long that different methylation states of H3K9 exist, and that these can instruct different repression mechanisms, it is not known whether these would define functionally distinct chromatin states that are physiologically relevant. Here we profiled H3K9me2 and H3K9me3 marks by ChIP-sequencing during meiosis and found that constitutive heterochromatin temporarily shifts to fully H3K9me3 marked nucleosomes, with little, if any, H3K9me2 left when cells exit mitosis and commit to the meiotic cell cycle. This H3K9 methylation switch is necessary for genome stability during gametogenesis, as cells lacking the ability to tri-methylate H3K9 exhibit chromosome segregation defects during MI and produce less viable spores. This is not the case during mitosis, explaining why the physiological relevance of H3K9me2 versus H3K9me3 states has remained obscure.

Such meiosis-specific importance of H3K9me3 is consistent with previous work demonstrating that centromeres are particularly

prone to disassembly during meiotic prophase. Reminiscent of transiently increasing Swi6 affinity through the herein reported H3K9 methylation switch, disassembly of centromeres during meiosis was shown to be counteracted by their transient localization in close proximity to the telomere bouquet, which may provide a suitable heterochromatin environment for centromere assembly, kinetochore remodeling, and monopolar attachment (Klutstein *et al*, 2015). Thus, high-affinity Swi6 binding sites and the increased local concentration of heterochromatin factors seem critical for enhancing the probability of correct assembly of meiotic centromeres.

The apparent chromosome segregation defect observed during MI of *clr4^{F449Y}/clr4^{F449Y}* cells is perplexing, because CenI-GFP dots had been shown to segregate normally during MI but not MII in the absence of Clr4 (Kitajima *et al*, 2003; Fig 3D). Notably, we rarely observed tetrads with two CenI-GFP dots in the same nucleus of a *clr4^{F449Y}* mutant, which would occur 50% of the time if segregation was random specifically in MII (Fig 3E). Thus, H3K9me2 appears sufficient to promote proper sister chromatid segregation during MII, alike in mitosis. However, a failure to convert H3K9me2 to H3K9me3 at the very beginning of meiosis manifests in aberrant MI chromosome segregation patterns later on. Because this is different in *clr4^A* cells, H3K9me2 may function in a dominant negative manner during this short window of time. Clearly, our mechanistic understanding of the role of heterochromatin during meiosis is far from complete, demanding further detailed mechanistic dissection experiments at the cell biology level, with temporal resolution and special attention to different methylation states of H3K9.

Towards achieving this goal, a better understanding of how Clr4 activities are controlled by the cell will mark an important step. We discovered that the ARL of Clr4 is phosphorylated in a Cdk1-dependent manner, which we propose functions to hold up the full transition from H3K9me2 to H3K9me3 during mitosis. Supporting this hypothesis, unphosphorylated Clr4 correlates with maximal H3K9me3 levels upon entry into meiosis, which can be mimicked in mitotic cells by inhibition of Cdk1. Inhibition of Cdk1 activity is essential for the initiation of sexual differentiation and early meiosis. Notably, nitrogen starvation induces a G₁ arrest, which is maintained by the Cdk1 inhibitor Rum1 (Stern & Nurse, 1998). Prior to premeiotic S-phase, Rum1 is degraded, upon which Cdk1 gets reactivated (Daga *et al*, 2003). This provides a likely mechanism underlying the premeiotic H3K9 methylation switch occurring at the very same time.

A limitation of our study is the lack of direct evidence that phosphorylation of Clr4 at S458 is indeed counteracting a full transition from H3K9me2 to H3K9me3. A commonly used strategy to address that problem would be the *in vivo* substitution of S458 with either a phospho-mimetic or a nonphosphorylatable amino acid (Dissmeyer & Schnittger, 2011). This is a powerful approach unless the mutated amino acid itself is crucial for the protein's function, irrespective of its phosphorylation state (Jonson & Petersen, 2001; Pérez-Mejías *et al*, 2020). This is of particular relevance if the respective residue is part of an exposed, unstructured loop, as is the case for S458 that resides in the ARL of Clr4 (Iglesias *et al*, 2018). Indeed, results that we have obtained with Alanine and Aspartate substitutions have remained inconclusive and prevent us from firmly concluding that S458 phosphorylation is directly involved in the regulation of Clr4. Thus, more sophisticated strategies, involving structure determination and *in vitro* reconstitution experiments, will be needed to prove causality.

Although these investigations need to be awaited, we note that Cdk1-dependent phosphorylation of the proline-directed serine within the SET and the post-SET domains of Clr4 appears to be conserved in the mammalian system. That is, SUV39H1^{S391}, analogous to Clr4^{S458}, is phosphorylated by CDK2 (Park *et al*, 2014). Whether SUV39H1 phosphoregulation could similarly affect methyltransferase specificity and is also controlling the faithful division of chromosomes during meiosis in humans remains to be investigated. If so, this could have key implications for understanding genetic disorders associated with aberrant chromosome segregation resulting in aneuploidy, such as Down syndrome or certain forms of cancer (Gordon *et al*, 2012).

Materials and Methods

Strains and plasmids

The diploid *h⁻/h⁻ pat1-as2/pat1-as2* strains were grown at 25°C in YE4S-ade. Cells carrying the *cdc2-as* mutation were grown at 25°C in YES. All other fission yeast strains were grown at 30°C in YES. All strains were constructed following the prevailing fission yeast protocol (Bähler *et al*, 1998) or by standard mating and sporulation. The Swi6-yeGFP fusion protein was tagged with a codon-optimized yeGFP-tag (Sheff & Thorn, 2004). Swi6 and yeGFP were separated by a “GDGAGLIN”-linker rendering the Swi6-yeGFP fusion protein functional (Keller *et al*, 2013; Stunnenberg *et al*, 2015). The diploid *h⁻/h⁻ pat1-as2/pat1-as2* strains were created by protoplast fusion (Ekwall & Thon, 2017). Strains and plasmids generated in this study are shown in Tables EV1 and EV2.

Synchronization of fission yeast meiosis

Fission yeast meiosis was synchronized as previously described (Cipak *et al*, 2014). Briefly, diploid *h⁻/h⁻ pat1-as2/pat1-as2* *S. pombe* cells were grown to OD₅₉₅ of 0.55 at 25°C in YE4S-ade. Cells were harvested (2,000 g, 2 min, 25°C), washed twice with sterile water, and resuspended in EMM2-NH₄Cl medium. Premeiotic nitrogen starvation was carried out for 7 h at 25°C (referred to as “0 h”). Afterward, cells were harvested (2,000 g, 2 min, 25°C), resuspended in EMM2 + NH₄Cl, and 25 μM 1-NM-PP1 (Toronto Research Chemicals) was added. The cell culture was grown at 25°C until the desired time points were reached.

Flow cytometry analysis of DNA content

One milliliter of cell culture (OD₅₉₅ of 0.55–1.2) was pelleted (4,000 g, 2 min, 4°C) and resuspended in 1 ml 70% ice-cold ethanol. Fixed cells were kept at 4°C if cells from multiple time points were collected. Five hundred microliter fixed cells were centrifuged (3,000 g, 5 min, 25°C) and washed twice with 1 ml 50 mM sodium citrate. Cell pellets were resuspended by vortexing. After the last washing step, pellets were treated with 500 μl 50 mM sodium citrate +0.1 mg/ml RNase A for at least 1.5 h at 37°C. Subsequently, 500 μl 50 mM sodium citrate +2 μM Sytox Green (Thermo Fisher Scientific) was added and samples were mixed by vortexing. To break apart cell aggregates, samples were sonicated for 5 s on a 550 Sonic Dismembrator (Thermo Fisher Scientific) before being

transferred to 5 ml FACS tubes (Becton Dickinson). Flow cytometry measurements were performed on a BD LSRII SORP Analyzer (Becton Dickinson) using a 488 nm excitation laser (flow rate = low; mode = linear). Per sample 20,000 cells were counted, and the data were postprocessed and visualized with FlowJo.

Chromatin immunoprecipitation

For H3K9me2, H3K9me3, and total H3 ChIP 50 ml of fission yeast culture were grown to mid-log phase (or synchronized as described before) and crosslinked with 1% formaldehyde (15 min, 25°C). For Swi6 ChIP, cells were incubated for 2 h at 18°C, resuspended in 5 ml PBS (1,761 g, 3 min, 18°C), double-crosslinked with 1.5 mM EGS (30 min, 25°C) and 1% formaldehyde (30 min, 25°C). The crosslinking reaction was quenched by the addition of 130 mM glycine (5 min, 25°C). Cells were washed twice (1,761 g, 4 min, 4°C) with 15 ml ice-cold PBS and transferred to a 2 ml screw cap tube with 500 µl ice-cold PBS. Cells were spun down (1,761 g, 3 min, 4°C), flash-frozen in liquid nitrogen, and stored at -80°C until use. For the ChIP, cell pellets were thawed on ice and resuspended in 400 µl ice-cold complete lysis buffer (50 mM HEPES/KOH pH 7.5, 140 mM NaCl, 1 mM EDTA, 1% Triton X-100, 0.1% sodium deoxycholate [fresh], 1× HALT protease inhibitor cocktail [Thermo Fisher Scientific]). Silica beads (0.5 mm) were added up to the meniscus of the cell suspension and cells were lysed at 4°C using a FastPrep-24 bead beating grinder (MP biomedical) (3× 60 s at 6.5 m/s). To prevent overheating during bead beating, the reaction tubes were cooled down for 2 min on ice between each round. The reaction tubes were punctured with a 25 G needle and the crude lysate was collected by centrifugation (196 g, 1 min, 4°C). The lysates were adjusted to 1.5 ml with complete lysis buffer in 15 ml Bioruptor Pico tubes (Diagenode) and sonicated for two rounds at 4°C (12 cycles, 30 s on/30 s off) using the Bioruptor Pico system (Diagenode). Samples were cooled down on ice for 5 min between each round. Afterward, lysates were cleared twice by centrifugation (15,700 g, 4°C) for 5 and 15 min, respectively. In the meantime, 2.5 µg of anti-H3K9me2 (MAB10307), anti-H3K9me3 (MAB10308), anti-histone H3 (ab1791), or anti-Swi6 (Stunnenberg *et al*, 2015) antibody was precoupled to either 30 µl anti-mouse IgG or anti-rabbit IgG dynabeads (Thermo Fisher Scientific) for 30 min at 25°C. The cleared lysates were normalized by total protein concentration and the conjugated dynabeads were added (2 h, 4°C). If needed, 50 µl of lysate was saved as an input control. The dynabeads were separated using a magnetic rack and washed three times with 1 ml ice-cold lysis buffer, once with 1 ml ice-cold wash buffer I (10 mM Tris-HCl pH 8.0, 250 mM LiCl, 0.5% NP-40, 0.5% sodium deoxycholate [fresh], 1 mM EDTA), and once with 1 ml ice-cold 1× TE. The ChIPs were eluted first in 100 µl 1% TES (1% SDS, 1× TE; 10 min, 65°C) and a second time in 150 µl 0.67% TES (0.67% SDS, 1× TE; 5 min, 65°C). The eluates were combined ($V_t = 250 \mu\text{l}$) and decrosslinked overnight at 65°C. Samples were treated with 40 µg RNase A (1 h, 37°C) and 60 µg Proteinase K (1 h, 65°C). DNA was precipitated by the addition of 150 mM NaCl and 1 volume isopropanol (15 min, 25°C), cleaned up using 30 µl AMPure XP beads, and eluted in 20 µl elution buffer (10 mM Tris-HCl pH 8.0, 1 mM EDTA).

For ChIP quantification with spike-ins, mESC were harvested, fixed, and lysed as described previously (Kaaij *et al*, 2019). 0.1%

mESC chromatin was added to the yeast lysates after cell lysis and the ChIP was carried out as described above.

Quantitative real-time PCR

ChIP DNA was diluted 1:20 and real-time PCR was performed using the SsoAdvanced SYBR Green supermix (Bio-Rad) and a CFX96 Real-Time System (Bio-Rad). Primer sequences of oligos used for qPCR are given in Table EV3.

Total RNA isolation and sequencing

Total RNA was extracted using the MasterPure Yeast RNA Purification kit (Lucigen). Libraries were prepared with the TruSeq Stranded Total RNA kit (Illumina) according to the manufacturer's instructions and sequenced with an Illumina HiSeq2500 (50 bp single-end). Reads were processed, normalized, and analyzed using QuasR with two mismatches allowed (Gaidatzis *et al*, 2015).

ChIP-sequencing

ChIP-sequencing libraries were generated using the NEBNext Ultra II DNA Library Prep Kit (New England Biolabs) and sequenced with an Illumina HiSeq2500 (50 bp single-end). Raw data were demultiplexed, converted to fastq format using bcl2fastq2 (v1.17), and mapped using STAR (Genome_build: Spombe.ASM294v2.24). For bigwig track generation by bedtools (v2.26.0) and bedGraphToBigWig (from UCSC binary utilities), nonaligned reads were discarded and read coverage was normalized to 1 million genome mapping reads (RPM). All ChIP-sequencing experiments were done at least twice, except the mouse ES cell spike-in ChIP-sequencing experiment, which was performed once. Initially, to account for potential ChIP efficiency differences between time points we compared the RPM normalization with normalization using spike-in chromatin. For ChIP quantification using the mESC spike-in chromatin, the ChIPs were mapped with STAR to both the *S. pombe* and the mouse mm10 genome assembly. The *S. pombe* H3K9me2 and H3K9me3 ChIP-sequencing read counts were then normalized to 1 million mapped mouse reads for each library to account for potential ChIP efficiency differences. This revealed that the normalization method did not change the results and we continued without spike-in normalization.

To generate the meiotic time course heat maps, H3K9me2 and H3K9me3 enrichments (IP/input) were normalized to histone H3 enrichments (IP/input). The respective replicates were averaged and plotted using the heatmap.2 function from the gplots package in R. Row Z-score normalization was performed within the heatmap.2 function (scale = "row").

Peakfinding for Swi6⁺ and Swi6^{Chp1-like-CD} was performed using MACS2 (v2.2.6) with default settings. Heterochromatic peaks were discarded, and the remaining euchromatic ChIP peak regions were extended/shortened to 1 kb around the peak center. These 1 kb peak windows were further used to count H3K9me2 and H3K9me3 ChIP reads. The RPM normalized read counts for the top 100 Swi6^{Chp1-like-CD} peaks windows were then used for visualization by boxplots.

To quantify gene expression changes under Swi6⁺ and Swi6^{Chp1-like-CD} peaks, the peak regions were intersected with gene

annotations and gene RPKM values of overlapping and nonoverlapping genes were plotted as boxplots in the respective genotypes.

Immunofluorescence microscopy

IF experiments were performed as described previously (Hagan, 2016) with minor modifications. In brief, to analyze mitotic chromosome segregation 10 ml yeast cultures were grown to mid-log phase and fixed with 3% formaldehyde and 0.25% glutaraldehyde (1 h, 25°C). To investigate chromosome segregation during MI, 10 ml of exponentially growing homothallic cells were harvested (1,761 g, 3 min, 25°C) and plated on a SPAS plate and incubated overnight (Forsburg & Rhind, 2006). The next day cells were scraped off, resuspended in 10 ml sterile water, and fixed as described before. Cells were permeabilized with 0.75 mg/ml lysing enzyme from *Trichoderma harzianum* (Sigma) and 0.375 mg/ml Zymolyase (Zymo Research) for 45 min at 25°C. 1:10 diluted TAT1 anti-tubulin tissue culture supernatant (00020911) was used as the primary antibody and 1:500 diluted Alexa Fluor 568-conjugated anti-mouse antibody (Thermo Fisher Scientific) was used as the secondary antibody. Cells were mounted on lectin-coated (Sigma) microscopy slides using SlowFade Gold Antifade Mountant with DAPI (Thermo Fisher Scientific). Images were acquired on an inverted AxioObserver7 microscope (Zeiss), equipped with a Yokogawa CSU W1-T2 spinning disk and a PlanApo 100×/1.40 oil objective, using the software Visiview. Z-stacks of cells exhibiting mitotic and meiotic spindles, respectively, were acquired and chromosome segregation was scored by the presence and absence of missegregating DAPI signal. Maximum intensity projections were created using FIJI.

Live cell imaging

One milliliter of exponentially growing homothallic *swi6-yeGFP mis6-mCherry* cells were harvested (1,761 g, 3 min, 25°C) and plated on a SPAS plate overnight. To follow the segregation of CenI-GFP, two heterothallic strains heterozygous for the mating type and the *cenI-GFP* marker were grown to the exponential phase and harvested as described above. Cells were mixed in water and plated on a SPAS plate for 1 or 2 days to analyze dyads and tetrads, respectively. Subsequently, cells were scraped off, resuspended in 500 μ l EMM2 + NH₄Cl, and mounted on lectin-coated (Sigma) microscopy slides. Images were acquired on an inverted AxioObserver7 microscope (Zeiss), equipped with a Yokogawa CSU W1-T2 spinning disk and a PlanApo 100×/1.40 oil objective, using the software Visiview. Z-stacks of either dyads or tetrads were acquired. Maximum intensity projections were created using FIJI.

Tetrad dissection and spore viability

Homothallic strains (spb594, spb3475, spb4712) were resuspended in 10 μ l sterile water, plated on SPAS plates, and incubated at 30°C for 2–3 days. Cells were scraped off and resuspended in 1 ml sterile water and asci formation was assessed by microscopy. Thirty microliter of a 1:100 tetrad asci dilution was dispersed on a YES plate and tetrads were separated with an MSM System (Singer Instruments). After 6 h at room temperature, spores were dissected and plates were incubated at 30°C to allow colony formation (4–5 days). Spore viability was assessed by distinguishing between tetrads that gave

rise to four colonies (4 colonies/tetrad) or less than four colonies (< 4 colonies/tetrad).

Generation of phospho-specific α -pS458 antibody

The “Phospho-Specific Antibody Services” of GenScript was used to generate the rabbit polyclonal anti-pS458 antibody. “CTFDYA-GAKDF(pS458)PVQ” was used as the antigen peptide.

Immunoprecipitation

Unless stated otherwise, all steps were carried out on ice (or at 4°C) and with ice-cold buffers. One hundred milliliter of fission yeast culture were grown to mid-log phase (or synchronized as described before) and pelleted (1,534 g, 4 min). Synchronized cultures were harvested in the presence of 1 mM PMSF. Pellets were washed twice with 5 ml TBS (50 mM Tris-HCl pH 7.5, 150 mM NaCl), resuspended in 500 μ l TBS, harvested (3,300 g, 30 s), and flash-frozen in liquid nitrogen. Cell pellets were stored at –80°C until use. For the IP, pellets were thawed on ice and resuspended in 400 μ l lysis buffer (20 mM HEPES/KOH pH 7.5, 500 mM NaCl, 5 mM MgCl₂, 1 mM EDTA, 10% glycerol, 0.25% Triton X-100, 0.5 mM DTT (fresh), 1× HALT protease and phosphatase inhibitor cocktail [Thermo Fisher Scientific]). Silica beads (0.5 mm) were added up to the meniscus of the cell suspension and cells were lysed using a FastPrep-24 bead beating grinder (MP biomedical; 3× 20 s at 6.5 m/s). To prevent overheating during bead beating, the reaction tubes were cooled down for 2 min on ice between each round. The reaction tubes were punctured with a 25 G needle and the crude lysate was collected by centrifugation (196 g, 1 min). The lysates were cleared twice by centrifugation (15,700 g, 10 min), and the protein concentration of the supernatant was estimated using a Bradford assay (Bio-Rad). Samples were normalized to 2–3 mg total protein in 800 μ l complete lysis buffer. 2.5 μ g anti-FLAG M2 antibodies (Sigma) were precoupled to 30 μ l anti-mouse IgG dynabeads (Thermo Fisher Scientific) for 30 min at 25°C and incubated for 2 h with the cell lysates. The dynabeads were separated using a magnetic rack and washed twice with 500 μ l complete lysis buffer and twice with 500 μ l wash buffer (20 mM HEPES/KOH pH 7.5, 150 mM NaCl, 5 mM MgCl₂, 10% glycerol, 0.25% Triton X-100). Depending on the downstream application, beads were treated differently from this point onwards.

Western blot

IP-dynabeads were boiled in 25 μ l 1× sample buffer (62.5 mM Tris-HCl pH 6.8, 10% glycerol, 2% SDS, 5% β -mercaptoethanol, 0.005% bromophenol blue) for 5 min at 95°C. Twelve microliter of the supernatant were loaded either on a Bolt 4–12% Bis-Tris gel (Thermo Fisher Scientific) or a SuperSep PhosTag gel (Wako). Gels were transferred using the Trans-Blot Turbo Transfer System (Bio-Rad). All steps were carried out according to the manufacturer's instructions.

Phosphatase assay

IP-dynabeads were transferred to a fresh reaction tube with 500 μ l B100-nd buffer (10 mM Tris-HCl pH 7.5, 2 mM MgCl₂, 100 mM

NaCl) and washed twice on a magnetic rack. The phosphatase assay was carried out using Lambda Protein Phosphatase (λ -PP) (New England Biolabs) according to the manufacturer's instructions. The reactions were performed in the presence and absence of λ -PP and 1 \times HALT phosphatase inhibitor cocktail (Thermo Fisher Scientific).

Mass spectrometry

IP-dynabeads were transferred to a fresh reaction tube with 500 μ l B100-nd buffer (10 mM Tris-HCl pH 7.5, 2 mM MgCl₂, 100 mM NaCl) and washed twice on a magnetic rack. Beads were digested for 2 h at 25°C with 0.2 μ g Lys-C in 5 μ l HTC buffer (20 mM HEPES/KOH pH 8.5, 5 mM TCEP, 10 mM CAA) containing 8 M urea. Subsequently, 17 μ l HEPES/KOH pH 8.5 and 0.2 μ g trypsin were added and the digestion reaction was incubated overnight at 37°C. Peptides generated by trypsin digestion were acidified with 0.8% TFA (final) and analyzed by LC-MS/MS on an EASY-nLC 1000 (Thermo Scientific) with a two-column set-up. The peptides were applied onto a peptide μ PACTM trapping column in 0.1% formic acid and 2% acetonitrile in H₂O at a constant flow rate of 5 μ l/min. Using a flow rate of 500 nl/min, peptides were separated at RT with a linear gradient of 3–6% buffer B in buffer A in 4 min followed by a linear increase from 6 to 22% in 55 min, 22–40% in 4 min, 40–80% in 1 min, and the column was finally washed for 10 min at 80% buffer B in buffer A (buffer A: 0.1% formic acid; buffer B: 0.1% formic acid in acetonitrile) on a 50 cm μ PACTM column (PharmaFluidics) mounted on an EASY-SprayTM source (Thermo Scientific) connected to an Orbitrap Fusion LUMOS (Thermo Scientific). The survey scan was performed using a 120,000 resolution in the Orbitrap. The PRM analysis was optimized using synthetic heavy peptides. The Clr4 peptides were targeted based on their retention times and fragmented using HCD followed by an orbitrap detection using a 120,000 resolution. The acquired PRM data were processed using Skyline 4 (MacLean et al, 2010). The transition selection was systematically verified and adjusted when necessary to ensure that no co-eluting contaminant was distorting the signal.

Whole-cell lysate extraction

Whole-cell lysates (WCL) for 3xFLAG-Clr4 detection were extracted as described previously (Krapp et al, 2019). For histone H3 and H3K9me3 detection, WCL was prepared using trichloroacetic acid (TCA).

In vitro kinase assays

Wild-type and mutant versions of Clr4KMT (catalytic domain containing residues 192–490) were purified as described previously (Stirpe et al, 2021). Briefly, HisSumo-Clr4KMT was expressed in *E. coli* and bound to a HisTrap column (GE Healthcare, cat no. 17-5247-01). Clr4KMT was separated from the HisSUMO tag by on-column cleavage, collected, and purified further by size exclusion chromatography using a Superdex 75 (GE Healthcare, cat no. 28989333) column. Kinase assays were performed by reacting 1 μ M Clr4KMT with 40 ng of human CDK1/Cyclin B (Thermo Fisher Invitrogen, cat no. PV3292) in 50 mM HEPES pH 7.6, 5 mM MgCl₂, 2 mM ATP for 2 h at 30°C. Reactions were

lyophilized and processed for LC-MS/MS analysis. Wild-type and mutant Clr4KMT samples were supplemented with HTC buffer, 0.2 μ g Lys-C and 0.2 μ g trypsin. The digestion reaction was carried out overnight at 37°C. Following the digestion, peptides were acidified with 0.8% TFA (final) and analyzed by LC-MS/MS using the MS system and the gradient described before. The DDA approach was used with the MS2 scans recorded in the ion trap detector. The MS raw files were processed using Maxquant software v1.5.3.8. The MS2 spectrum was searched against *S. pombe* uniprot database (downloaded 2019/04/10) including pS and pT as variable modifications.

Statistics

Global variance of the meiotic time course ChIP-qPCR data were assessed using ANOVA. For statistical analysis of ChIP-qPCR data a two-tailed Student's *t*-test was used. The significance of chromosome segregation, CenI-GFP segregation, and spore viability was determined with a Fisher's exact test. In all cases, $P < 0.05$ was used as the significance level. No statistical methods were used to pre-determine the sample size.

Data availability

All custom codes used to analyze data and generate figures are available upon reasonable request.

- RNA-Seq data: Gene Expression Omnibus [GSE182250](https://www.ncbi.nlm.nih.gov/geo/query/acc.cgi?acc=GSE182250) (<https://www.ncbi.nlm.nih.gov/geo/query/acc.cgi?acc=GSE182250>).
- Chip-Seq data: Gene Expression Omnibus [GSE182250](https://www.ncbi.nlm.nih.gov/geo/query/acc.cgi?acc=GSE182250) (<https://www.ncbi.nlm.nih.gov/geo/query/acc.cgi?acc=GSE182250>).

Expanded View for this article is available [online](#).

Acknowledgements

We thank Fabio Mohn for discussion, advise, data analysis, data deposition, and feedback on the manuscript. We thank Yukiko Shimada and Nathalie Laschet for technical support and Max Louski for his contribution to generating strains. We would like to thank the FMI Functional Genomics facility for assistance in library construction and next-generation sequencing and Jan Seebacher for discussions. We are grateful to Laurent Gelman and Steven Bourke for assistance during imaging, and we thank Juraj Gregan and Viesturs Simanis for sharing strains. Also, we thank Viesturs Simanis for commenting on the manuscript. This work has received funding from the European Research Council (ERC) under the European Union's Horizon 2020 research and innovation program (grant agreement no. 681213 - REpiReg), the Novartis Research Foundation, and the Biotechnology and Biological Sciences Research Council (BB/S018549).

Author contributions

Marc Buehler: Conceptualization; resources; supervision; funding acquisition; visualization; writing—original draft; project administration; writing—review and editing. **Tahsin Kuzdere:** Conceptualization; formal analysis; validation; investigation; visualization; methodology; writing—original draft; writing—review and editing. **Valentin Flury:** Conceptualization; supervision; methodology. **Thomas Schallch:** Investigation. **Vytautas Iesmantavicius:** Formal analysis; investigation. **Daniel Hess:** Formal analysis; investigation.

Disclosure and competing interests statement

The authors declare competing financial interests: FMI receives significant financial contributions from the Novartis Research Foundation. Published research reagents from the FMI are shared with the academic community under a Material Transfer Agreement (MTA) having terms and conditions corresponding to those of the UBMTA (Uniform Biological Material Transfer Agreement). Correspondence and requests for materials should be addressed to marc.buehler@fmi.ch.

References

- Allshire RC, Ekwall K (2015) Epigenetic regulation of chromatin states in *Schizosaccharomyces pombe*. *Cold Spring Harb Perspect Biol* 7: a018770
- Bähler J, Wu JQ, Longtine MS, Shah NG, McKenzie A 3rd, Steever AB, Wach A, Philippsen P, Pringle JR (1998) Heterologous modules for efficient and versatile PCR-based gene targeting in *Schizosaccharomyces pombe*. *Yeast* 14: 943–951
- Bannister AJ, Zegerman P, Partridge JF, Miska EA, Thomas JO, Allshire RC, Kouzarides T (2001) Selective recognition of methylated lysine 9 on histone H3 by the HP1 chromo domain. *Nature* 410: 120–124
- Bernard P, Maure J-F, Partridge JF, Genier S, Javerzat J-P, Allshire RC (2001) Requirement of heterochromatin for cohesion at centromeres. *Science* 294: 2539–2542
- Bloom KS (2014) Centromeric heterochromatin: the primordial segregation machine. *Annu Rev Genet* 48: 1–28
- Carpay A, Krug K, Graf S, Koch A, Popic S, Hauf S, Macek B (2014) Absolute proteome and phosphoproteome dynamics during the cell cycle of *Schizosaccharomyces pombe* (fission yeast)*. *Mol Cell Proteomics* 13: 1925–1936
- Chikashige Y, Ding D, Funabiki H, Haraguchi T, Mashiko S, Yanagida M, Hiraoka Y (1994) Telomere-led premeiotic chromosome movement in fission yeast. *Science* 264: 270–273
- Cipak L, Polakova S, Hyppa RW, Smith GR, Gregan J (2014) Synchronized fission yeast meiosis using an ATP analog-sensitive Pat1 protein kinase. *Nat Protoc* 9: 223–231
- Daga RR, Bolaños P, Moreno S (2003) Regulated mRNA stability of the Cdk inhibitor Rum1 links nutrient status to cell cycle progression. *Curr Biol* 13: 2015–2024
- Dischinger S, Krapp A, Xie L, Paulson JR, Simanis V (2008) Chemical genetic analysis of the regulatory role of Cdc2p in the *S. pombe* septation initiation network. *J Cell Sci* 121: 843–853
- Dissmeyer N, Schnittger A (2011) Plant kinases, methods and protocols. *Methods Mol Biol* 779: 93–138
- Duempelmann L, Mohn F, Shimada Y, Oberti D, Andriollo A, Lochs S, Bühler M (2019) Inheritance of a phenotypically neutral epimutation evokes gene silencing in later generations. *Mol Cell* 74: 534–541.e4
- Eissenberg JC (2012) Structural biology of the chromodomain: form and function. *Gene* 496: 69–78
- Ekwall K, Thon G (2017) Setting up *Schizosaccharomyces pombe* crosses/ Matings. *Cold Spring Harb Protoc* 2017: pdb.prot091694
- Ekwall K, Javerzat J-P, Lorentz A, Schmidt H, Cranston G, Allshire R (1995) The chromodomain protein Swi6: a key component at fission yeast centromeres. *Science* 269: 1429–1431
- Ekwall K, Nimmo E, Javerzat J, Borgström B, Egel R, Cranston G, Allshire R (1996) Mutations in the fission yeast silencing factors *clr4⁺* and *rik1⁺* disrupt the localisation of the chromo domain protein Swi6p and impair centromere function. *J Cell Sci* 109: 2637–2648
- Ellermeier C, Higuchi EC, Phadnis N, Holm L, Geelhood JL, Thon G, Smith GR (2010) RNAi and heterochromatin repress centromeric meiotic recombination. *Proc Natl Acad Sci USA* 107: 8701–8705
- Forsburg SL, Rhind N (2006) Basic methods for fission yeast. *Yeast* 23: 173–183
- Gaidatzis D, Lerch A, Hahne F, Stadler MB (2015) QuasR: quantification and annotation of short reads in R. *Bioinformatics* 31: 1130–1132
- Gordon DJ, Resio B, Pellman D (2012) Causes and consequences of aneuploidy in cancer. *Nat Rev Genet* 13: 189–203
- Grewal SIS, Jia S (2007) Heterochromatin revisited. *Nat Rev Genet* 8: 35–46
- Hagan IM (2016) Immunofluorescence microscopy of *Schizosaccharomyces pombe* using chemical fixation. *Cold Spring Harb Protoc* 2016: pdb.prot091017
- Hall IM, Noma K, Grewal SIS (2003) RNA interference machinery regulates chromosome dynamics during mitosis and meiosis in fission yeast. *Proc Natl Acad Sci USA* 100: 193–198
- Iglesias N, Currie MA, Jih G, Paulo JA, Siuti N, Kalocsay M, Gygi SP, Moazed D (2018) Automethylation-induced conformational switch in Clr4 (Suv39h) maintains epigenetic stability. *Nature* 560: 504–508
- Jih G, Iglesias N, Currie MA, Bhanu NV, Paulo JA, Gygi SP, Garcia BA, Moazed D (2017) Unique roles for histone H3K9me states in RNAi and heritable silencing of transcription. *Nature* 547: 463–467
- Jonson PH, Petersen SB (2001) A critical view on conservative mutations. *Protein Eng Des Sel* 14: 397–402
- Keller C, Kulasegaran-Shyliani R, Shimada Y, Hotz H-R, Bühler M (2013) Noncoding RNAs prevent spreading of a repressive histone mark. *Nat Struct Mol Biol* 20: 994–1000
- Kettenbach AN, Deng L, Wu Y, Baldissard S, Adamo ME, Gerber SA, Moseley JB (2015) Quantitative phosphoproteomics reveals pathways for coordination of cell growth and division by the conserved fission yeast kinase Pom1*. *Mol Cell Proteomics* 14: 1275–1287
- Kitajima TS, Yokobayashi S, Yamamoto M, Watanabe Y (2003) Distinct Cohesin complexes organize meiotic chromosome domains. *Science* 300: 1152–1155
- Klutstein M, Fennell A, Fernández-Álvarez A, Cooper JP (2015) The telomere bouquet regulates meiotic centromere assembly. *Nat Cell Biol* 17: 458–469
- Krapp A, Hamelin R, Armand F, Chiappe D, Krapp L, Cano E, Moniatte M, Simanis V (2019) Analysis of the *S. pombe* meiotic proteome reveals a switch from anabolic to catabolic processes and extensive post-transcriptional regulation. *Cell Rep* 26: 1044–1058.e5
- Lachner M, Jenuwein T (2002) The many faces of histone lysine methylation. *Curr Opin Cell Biol* 14: 286–298
- Kaaij LJ, Mohn F, van der Weide RH, de Wit E, Bühler M (2019) The ChAHP complex counteracts chromatin looping at CTCF sites that emerged from SINE expansions in mouse. *Cell* 178: 1437–1451.e14
- MacLean B, Tomazela DM, Shulman N, Chambers M, Finney GL, Frewen B, Kern R, Tabb DL, Liebler DC, MacCoss MJ (2010) Skyline: an open source document editor for creating and analyzing targeted proteomics experiments. *Bioinformatics* 26: 966–968
- Martin C, Zhang Y (2005) The diverse functions of histone lysine methylation. *Nat Rev Mol Cell Biol* 6: 838–849
- Mata J, Lyne R, Burns G, Bähler J (2002) The transcriptional program of meiosis and sporulation in fission yeast. *Nat Genet* 32: 143–147
- Nabeshima K, Nakagawa T, Straight AF, Murray A, Chikashige Y, Yamashita YM, Hiraoka Y, Yanagida M (1998) Dynamics of centromeres during metaphase-anaphase transition in fission yeast: Dis1 is implicated in force balance in metaphase bipolar spindle. *Mol Biol Cell* 9: 3211–3225

- Nonaka N, Kitajima T, Yokobayashi S, Xiao G, Yamamoto M, Grewal SIS, Watanabe Y (2002) Recruitment of cohesin to heterochromatic regions by Swi6/HP1 in fission yeast. *Nat Cell Biol* 4: 89–93
- Olsen JV, Blagoev B, Gnäd F, Macek B, Kumar C, Mortensen P, Mann M (2006) Global, in vivo, and site-specific phosphorylation dynamics in signaling networks. *Cell* 127: 635–648
- Park SH, Yu SE, Chai YG, Jang YK (2014) CDK2-dependent phosphorylation of Suv39H1 is involved in control of heterochromatin replication during cell cycle progression. *Nucleic Acids Res* 42: 6196–6207
- Pérez-Mejías G, Velázquez-Cruz A, Guerra-Castellano A, Baños-Jaime B, Díaz-Quintana A, González-Arzola K, la Mád R, Díaz-Moreno I (2020) Exploring protein phosphorylation by combining computational approaches and biochemical methods. *Comput Struct Biotechnol J* 18: 1852–1863
- Pidoux AL, Uzawa S, Perry PE, Cande WZ, Allshire RC (2000) Live analysis of lagging chromosomes during anaphase and their effect on spindle elongation rate in fission yeast. *J Cell Sci* 113: 4177–4191
- Schalch T, Job G, Noffsinger VJ, Shanker S, Kuscu C, Joshua-Tor L, Partridge JF (2009) High-affinity binding of Chp1 chromodomain to K9 methylated histone H3 is required to establish centromeric heterochromatin. *Mol Cell* 34: 36–46
- Sheff MA, Thorn KS (2004) Optimized cassettes for fluorescent protein tagging in *Saccharomyces cerevisiae*. *Yeast* 21: 661–670
- Stern B, Nurse P (1998) Cyclin B proteolysis and the cyclin-dependent kinase inhibitor rum1p are required for pheromone-induced G1 arrest in fission yeast. *Mol Biol Cell* 9: 1309–1321
- Stirpe A, Guidotti N, Northall SJ, Kilic S, Hainard A, Vadas O, Fierz B, Schalch T (2021) SUV39 SET domains mediate crosstalk of heterochromatic histone marks. *Elife* 10: e62682
- Stunnenberg R, Kulasegaran-Shylini R, Keller C, Kirschmann MA, Gelman L, Bühler M (2015) H3K9 methylation extends across natural boundaries of heterochromatin in the absence of an HP1 protein. *EMBO J* 34: 2789–2803
- Swaffer MP, Jones AW, Flynn HR, Snijders AP, Nurse P (2018) Quantitative phosphoproteomics reveals the signaling dynamics of cell-cycle kinases in the fission yeast *Schizosaccharomyces pombe*. *Cell Rep* 24: 503–514
- Watanabe Y, Nurse P (1999) Cohesin Rec8 is required for reductional chromosome segregation at meiosis. *Nature* 400: 461–464
- Yamagishi Y, Sakuno T, Shimura M, Watanabe Y (2008) Heterochromatin links to centromeric protection by recruiting shugoshin. *Nature* 455: 251–255
- Yamashita A, Sakuno T, Watanabe Y, Yamamoto M (2017) Analysis of *Schizosaccharomyces pombe* meiosis. *Cold Spring Harb Protoc* 2017: pdb.top079855



License: This is an open access article under the terms of the [Creative Commons Attribution](https://creativecommons.org/licenses/by/4.0/) License, which permits use, distribution and reproduction in any medium, provided the original work is properly cited.